



Nanoscale

**Bidirectional tuning of phase transition properties in Pt: VO<sub>2</sub> nanocomposite thin films**

Journal:	<i>Nanoscale</i>
Manuscript ID	NR-ART-05-2020-004008.R1
Article Type:	Paper
Date Submitted by the Author:	22-Jul-2020
Complete List of Authors:	<p>He, Zihao; Purdue University          Jian, Jie; Purdue University          Misra, Shikhar; Purdue University          Gao, Xingyao; Purdue University          Wang, Xuejing; Purdue University System, MSE          Qi, Zhimin; Purdue University System          Yang, Bo; Purdue University System          Zhang, Di; Purdue University, School of Materials Engineering          Zhang, Xinghang; Purdue University System, Materials Engineering          Wang, Haiyan; Purdue University System, MSE; Neil Armstrong          Engineering Building</p>

SCHOLARONE™  
Manuscripts

**Bidirectional tuning of phase transition properties in Pt: VO<sub>2</sub> nanocomposite thin films**

*Zihao He<sup>a</sup>, Jie Jian<sup>b</sup>, Shikhar Misra<sup>b</sup>, Xingyao Gao<sup>b</sup>, Xuejing Wang<sup>b</sup>, Zhimin Qi<sup>b</sup>, Bo Yang<sup>b</sup>, Di Zhang<sup>b</sup>, Xinghang Zhang<sup>b</sup>, Haiyan Wang<sup>a,b\*</sup>*

<sup>a</sup> School of Electrical and Computer Engineering, Purdue University, West Lafayette, IN 47907-2045, United States

<sup>b</sup> School of Materials Engineering, Purdue University, West Lafayette, IN 47907-2045, United States

\* Author to whom correspondence should be addressed. E-mail: [hwang00@purdue.edu](mailto:hwang00@purdue.edu)

**Keywords:** pulsed laser deposition, vanadium dioxide, metal-oxide nanocomposites, semiconductor metal transition, band structure reconstruction

**Abstract**

Phase transition material VO<sub>2</sub> with a semiconductor-to-metal transition (SMT) near 341 K (68 °C) has attracted significant research interests because of its drastic change in electrical resistivity and optical dielectric properties. To address its application needs at specific temperatures, tunable SMT temperatures are highly desired. In this work, effective transition temperature ( $T_c$ ) tuning of VO<sub>2</sub> has been demonstrated via a novel Pt: VO<sub>2</sub> nanocomposite design, i.e., uniform Pt nanoparticles (NPs) embedded in the VO<sub>2</sub> matrix. Interestingly, a bidirectional tuning has been achieved, i.e., the transition temperature can be systematically tuned to as low as 329.16 K, or as high as 360.74 K with the average diameter of Pt NPs increasing from 1.56 to 4.26 nm. Optical properties, including transmittance ( $T\%$ ) and dielectric permittivity ( $\epsilon'$ ) were all effectively tuned accordingly. All Pt: VO<sub>2</sub> nanocomposite thin films maintain reasonable SMT properties, i.e. sharp phase transition and narrow width of thermal hysteresis. The bidirectional  $T_c$  tuning is attributed to two factors: the reconstruction of band structure at the Pt: VO<sub>2</sub> interface and the change of Pt: VO<sub>2</sub> phase boundary density. This demonstration sheds light on phase transition tuning of VO<sub>2</sub> towards both room temperature and high temperature end, which provides a promising approach for VO<sub>2</sub>-based novel electronics and photonics operating under specific temperatures.

## Introduction

Mott metal-insulator phase transition has been widely studied in metal oxides owing to their abrupt changes in physical properties during phase transition.<sup>1</sup> Such changes arise due to the electron-electron interaction effect<sup>2</sup> and are for potential applications in memory and switching devices.<sup>3</sup> One such Mott transition material is vanadium dioxide (VO<sub>2</sub>), which has been a centerpiece of transition metal oxides research over the past decade, because of its ultrafast and reversible phase transition around 341 K.<sup>4-6</sup> The room-temperature semiconductor phase VO<sub>2</sub> has a monoclinic crystal structure. By the reversible first-order semiconductor-to-metal transition (SMT), semiconductor phase VO<sub>2</sub> transforms into a tetragonal rutile crystal structure.<sup>7,8</sup> Such phase transition drastically changes its electrical and optical properties, with an electrical resistivity transition of 4-5 orders of magnitude<sup>9</sup> and optical transmission transition of 40-50% in the near infrared and terahertz wavelength region.<sup>10</sup> The resulting functional property tuning presents a wide variety of applications involving optical and electrical based sensing and switching devices, including memristor,<sup>11</sup> chemical and biological sensors,<sup>12</sup> intelligent window coatings,<sup>13</sup> and switching materials.<sup>14</sup>

It is attractive to tailor the phase transition temperature ( $T_c$ ) of VO<sub>2</sub> thin films to satisfy a specific working temperature. Thus recent efforts have been devoted towards the realization of  $T_c$  tuning of VO<sub>2</sub> films for potential device applications.  $T_c$  tuning of VO<sub>2</sub> has been mainly achieved using doping and strain engineering. Specifically, by introducing different substrates and buffer layers,  $T_c$  of VO<sub>2</sub> films can either be tuned up or down due to the strain from the lattice misfit between the film and the substrate.<sup>15-17</sup> However, large strain is usually accompanied with high defect densities.<sup>18,19</sup> Alternatively, a number of dopants, including Mg, W, Al, Cr, and Nb, were reported to successfully tune the transition temperature of VO<sub>2</sub> films from 308 to 384 K.<sup>20-23</sup>

However, the increase of doping level could cause the degradation of phase transition properties due to consequent defects<sup>24</sup> and multivalent vanadium ions.<sup>25</sup>

Recently, a VO<sub>2</sub>-metal nanocomposite design was proposed as a novel approach to overcome the abovementioned degradation.<sup>26,27</sup> Depending on the work function of different metals, tunability of  $T_c$  could be achieved primarily by the alignment of Fermi level of VO<sub>2</sub> and embedded metal nanoparticles (NPs). Au NPs was first introduced for  $T_c$  tuning of VO<sub>2</sub> towards room temperature applications.<sup>26</sup> SMT in Au:VO<sub>2</sub> nanocomposite films was tuned by charge-transfer-induced bandwidth control. The effective tuning of VO<sub>2</sub> phase transition properties was later experimentally demonstrated using metals with different work function, and a record low  $T_c$  of 301.8 K was achieved with high film quality and reasonable SMT performance.<sup>27</sup>

In this work, we propose to achieve the effective  $T_c$  tuning of VO<sub>2</sub> films via a single metal selection, considering that the work function of many metal NPs is size dependent and thus can be used to tune the  $T_c$  of VO<sub>2</sub>.<sup>28</sup> More specifically, a bidirectional  $T_c$  tuning of VO<sub>2</sub> films is proposed via a novel Pt: VO<sub>2</sub> nanocomposite design. As illustrated in **Figure 1**, Pt NPs with various NP sizes are uniformly embedded in the VO<sub>2</sub> matrix using a single-step pulsed laser deposition (PLD) method. Pt was selected due to its size dependent work function. Interestingly, the work function of Pt NPs can go across the work function of VO<sub>2</sub> via size tuning. Therefore, the conduction band of VO<sub>2</sub> can be bent either upwards or downwards for  $T_c$  tuning upon forming Schottky junction with the metal phase.<sup>5</sup> The proposed NP size control can be realized via deposition temperature variation. Through the NP size tuning, it is possible to achieve tunable phase transition properties and optical properties and thus the transport properties, optical transmittance, dielectric permittivity, and epsilon-near-zero (ENZ) wavelength of the samples were measured and correlated with the Pt: VO<sub>2</sub> structures.

## Experimental

Pt: VO<sub>2</sub> nanocomposite thin films were deposited onto c-cut sapphire substrates using pulsed laser deposition (PLD, KrF excimer laser,  $\lambda = 248$  nm). The laser beam was incident at an angle of 45° to achieve an approximate energy density of 3 J/cm<sup>2</sup>. The laser beam was aligned to maintain comparable Pt/V compositions of all films deposited at different temperature. V<sub>2</sub>O<sub>5</sub> target, which was pressed and sintered by conventional method, was used for Pt: VO<sub>2</sub> nanocomposite thin film deposition along with the Pt strip. All films were deposited with constant oxygen pressure (0.01 Torr) and laser frequency (2 Hz). The deposition temperatures were ranged from 500 to 650°C to control the size of Pt NPs.

The microstructures of Pt: VO<sub>2</sub> thin films were characterized through X-ray diffraction (XRD, PANalytical Empyrean with Cu K $\alpha$  radiation), selected-area electron diffraction (SAED) pattern, scanning transmission electron microscopy (STEM, Thermo Scientific TALOS F200X), energy dispersive X-ray spectroscopy (EDS) and high resolution STEM (HR-STEM). The phase transition of Pt: VO<sub>2</sub> thin films was studied using in-situ high temperature XRD (PANalytical Empyrean with DHS 1100 domed heating stage). The HR-STEM images in high-angle annular dark-field (HAADF) mode were acquired by Thermo Scientific Themis Z with a Cs probe corrector operated at 200kV. Cross-sectional TEM samples were prepared via a standard grinding procedure, involving manual grinding, polishing, dimpling, and a final ion-milling step (PIPS 695 precision ion polishing system, 5 keV). The composition of nanocomposite thin films was characterized using large-scale EDS quantification in Quanta 600 scanning electron microscope (SEM). The electrical resistance of the nanocomposite thin films was investigated in a physical property measurement system (PPMS, Quantum Design DynaCool) with temperature ranging from 290 to 390 K. The dielectric permittivity of the as-deposited nanocomposite thin films was

measured using angular dependent spectroscopic ellipsometer (RC2 ellipsometer, J.A. Woollam) at three different angles of incidence ( $55^\circ$ ,  $65^\circ$ ,  $75^\circ$ ), both at room temperature ( $25^\circ\text{C}$ ) and elevated temperature ( $90^\circ\text{C}$ ). Normal incident depolarized transmittance ( $T\%$ ) measurement of the as-deposited nanocomposite thin films was carried out on an optical spectrophotometer (PerkinElmer LAMBDA 1050 UV/Vis spectrophotometer).

## Results and discussion

**Figure 1a** compares the XRD  $\theta$ - $2\theta$  scans of Pt: VO<sub>2</sub> nanocomposite thin films on c-cut sapphire substrates deposited under three different temperatures: 500, 600, and 650 °C. All the samples show the presence of VO<sub>2</sub> (M1) (020) peak, which suggests a highly textured b-axis growth of VO<sub>2</sub> matrix on c-cut sapphire. The peak positions of VO<sub>2</sub> (M1) (020) peak in all Pt: VO<sub>2</sub> films shift slightly to the left with respect to the pure VO<sub>2</sub> (M1) (020) peak. The result confirms the monoclinic phase VO<sub>2</sub> in all Pt: VO<sub>2</sub> films. The VO<sub>2</sub> (011)  $\phi$ -scans of Pt: VO<sub>2</sub> thin films (**Figure S1a, b**, supporting information) show three sets of peaks with an in-between rotation of  $60^\circ$ . In contrast, no obvious peak was observed in the VO<sub>2</sub> (102)  $\phi$ -scan. The  $\phi$ -scan results further support the VO<sub>2</sub> (M1) (020) out-of-plane growth on c-cut sapphire. However, the VO<sub>2</sub> peak intensities decrease gradually under higher temperatures, which suggests lower film texturing quality at higher temperatures. In addition, XRD spectrum of Pt: VO<sub>2</sub> film deposited at 650 °C shows an overlap between Pt (111) peak and VO<sub>2</sub> (M1) (020) peak, suggesting a (111) out-of-plane preferred growth of Pt NPs in the VO<sub>2</sub> matrix. Moreover, the peak positions of VO<sub>2</sub> (020) in all Pt: VO<sub>2</sub> films ( $\approx 39.91^\circ$ ) are very close to the bulk VO<sub>2</sub> (020) peak position ( $\approx 39.97^\circ$ , the black dashed line in **Figure 1a**), suggesting no major peak shift for films deposited at different temperatures. The result indicates no obvious strain between the VO<sub>2</sub> matrix and the sapphire substrate, which

is possibly due to the incorporation of Pt NPs in the VO<sub>2</sub> matrix. To study the phase transition in Pt: VO<sub>2</sub> films,  $\phi$ -scans using in-situ heating XRD for the 500 °C deposited Pt: VO<sub>2</sub> films were performed at room temperature (25 °C) and elevated temperature (90 °C). As shown in **Figure 1b**, the low-temperature monoclinic VO<sub>2</sub> (M1) (011) peak was replaced by the tetragonal rutile VO<sub>2</sub> (R) (110) peak at high temperature, confirming the M1-to-R phase transition for the Pt: VO<sub>2</sub> films.

The STEM cross-section images for Pt: VO<sub>2</sub> films deposited at 500, 600, and 650 °C are shown in **Figure 1b2, c2 and d2**, respectively. Pt NPs were uniformly distributed into the VO<sub>2</sub> matrix, and a thin layer of Pt was observed in all Pt: VO<sub>2</sub> films near the interface of film and substrate. The Pt layer near the film/substrate interface is very thin (~1nm) compared to the films (~70-80nm), and could serve as nucleation sites during deposition. All as-deposited films have similar thickness around 75 nm. Interestingly, the average Pt NPs diameter, as shown in Figure S2e, exhibits an obvious increase with the increase in deposition temperature. The average Pt NPs diameters (Figure S2, the supporting information) were measured as 1.56, 3.36 and 4.26 nm for films deposited at 500, 600, and 650 °C, respectively. The SAED pattern of the film/substrate interface area for 500 °C deposited Pt: VO<sub>2</sub> films, as shown in Figure S2d, was taken from c-cut sapphire [10 $\bar{1}$ 0] zone. Orientation relationships of VO<sub>2</sub> (020) // Al<sub>2</sub>O<sub>3</sub> (000 $\bar{6}$ ) and VO<sub>2</sub> (002) // Al<sub>2</sub>O<sub>3</sub> (1 $\bar{2}$ 10) can be determined from the diffraction pattern, which further confirms the monoclinic structure of VO<sub>2</sub> at room temperature and the highly textured growth of the Pt: VO<sub>2</sub> films. The Pt/V atomic ratio was derived for all Pt: VO<sub>2</sub> films using large-scale EDX mapping data in SEM (Figure S3, supporting information). The result confirms comparable Pt/V atomic ratio (21 $\pm$ 1%) for all the Pt: VO<sub>2</sub> nanocomposite thin films under deposition temperature ranging from 500 to 650 °C.

Atomic-level microstructure of Pt: VO<sub>2</sub> thin film deposited at 650 °C was characterized using high resolution STEM (HR-STEM), to investigate the interfacial coupling between Pt NPs and the VO<sub>2</sub> matrix. The STEM cross-section image in **Figure 2b** shows that Pt NPs were uniformly distributed into the VO<sub>2</sub> matrix. Pt (111) planes are along the out-of-plane orientation, as illustrated in **Figure 2c**, suggesting Pt (111) textured growth in VO<sub>2</sub> matrix. The result agrees with the XRD  $\theta-2\theta$  spectrum of Pt: VO<sub>2</sub> film deposited at 650 °C. Since Pt has a face centered cubic structure, VO<sub>2</sub> has a tetragonal rutile structure at deposition temperature and sapphire has a hexagonal structure, Pt NPs tend to have (111) textured growth considering the lattice matching between the Pt NPs, the matrix and the substrate. On the other hand, the Pt (111) out-of-plane preferred growth is also attributed to the lowest surface energy of the Pt (111) plane among all the major Pt surface planes, as reported previously.<sup>29</sup> The energy dispersive X-ray spectroscopy (EDS) mapping in **Figure 2d**, e and f confirms the uniform distribution of Pt NPs in the VO<sub>2</sub> matrix. Moreover, the inter-diffusion between metal phase and VO<sub>2</sub> matrix is restricted. In other words, Pt ad-atoms tend to form NPs on Pt nuclei rather than forming alloy with VO<sub>2</sub> matrix. The inter-diffusion is limited because of high thermal stability of metal phase and the high kinetic energy from laser system. A weak V signal was detected in areas where Pt NPs were present as shown in **Figure 2d**. It was further noted from **Figure 2f** that Pt NPs show no obvious oxidation owing to high oxidation resistance of metal phase.

The semiconductor-to-metal phase transition (SMT) properties of all Pt: VO<sub>2</sub> films deposited at different temperatures were characterized by R-T measurements. **Figure 3a** shows the normalized electrical resistance,  $\rho = R(T)/R(390\text{ K})$ , of pure VO<sub>2</sub> film and Pt: VO<sub>2</sub> films as a function of temperature. All SMT parameters in **Table 1**, including transition temperature ( $T_c$ ), transition amplitude ( $\Delta A$ ), transition sharpness ( $\Delta T$ ), and the width of thermal hysteresis ( $\Delta H$ ), are

calculated and summarized from the derivation of  $\log_{10}(\rho)$  versus temperature plot as shown in **Figure 3b-e**. Since  $T_c$  of pure VO<sub>2</sub> films deposited on c-cut sapphire have similar values (345.78 K) in prior work,<sup>27</sup> 500 °C deposited pure VO<sub>2</sub> film was used here as a reference. Compared to the pure VO<sub>2</sub> film deposited at 500 °C, the transition curve of Pt: VO<sub>2</sub> film deposited with the same parameter drastically shifts to the lower temperature end, with  $T_c$  decrease by 16.56 K to 329.16 K (56.16 °C). In contrast, the transition curve of the Pt: VO<sub>2</sub> films deposited at higher temperatures (600 and 650 °C) obviously shifts to the higher temperature end, with  $T_c$  increase by 9.55 K to 355.27 K (82.27 °C) and by 15.02 K to 360.74 K (87.74 °C), for Pt: VO<sub>2</sub> films deposited at 600 and 650 °C, respectively. As for SMT properties comparison, the transition sharpness ( $\Delta T$ ) increases for Pt: VO<sub>2</sub> film deposited at 500 °C. The broadening of  $\Delta T$  is related to high defect density at low deposition temperature.<sup>30</sup> In the meantime, both transition amplitude ( $\Delta A$ ) and the width of thermal hysteresis ( $\Delta H$ ) decrease at lower deposition temperature. The degradation of amplitude is possibly due to the increase of defect content near the grain boundaries,<sup>30</sup> while narrower thermal hysteresis is related to lower interfacial energy and smaller vertical grain boundaries as reported previously.<sup>31</sup> Compared to the pure VO<sub>2</sub> film deposited at 500 °C, Pt: VO<sub>2</sub> film deposited at same temperature has significantly lower resistance, indicating much improved film conductivity with the Pt NPs introduction. It is noted that, Pt: VO<sub>2</sub> film deposited at lower temperature shows smaller resistance value, suggesting improved film charge carrier density due to smaller Pt NPs. SMT measurements demonstrate high quality of Pt: VO<sub>2</sub> films with reasonable transition properties compared to pure VO<sub>2</sub> film.

The bidirectional tuning of  $T_c$  with different size of Pt NPs is mainly attributed to two factors: the reconstruction of band structure at the Pt: VO<sub>2</sub> interface and the change of Pt: VO<sub>2</sub> phase boundary density. Initially, VO<sub>2</sub> matrix forms a Schottky junction upon contact with the

metal phase, thereby reconstructing the energy band structure. Though the work function of bulk Pt is  $\sim 5.6$  eV,<sup>32</sup> which is larger than that of VO<sub>2</sub>  $\sim 5$  eV,<sup>33</sup> the size-dependent work function of Pt NPs can deviate strongly from that of bulk Pt due to the electrostatic interactions with the adjacent VO<sub>2</sub> matrix.<sup>34,35</sup> Since smaller Pt NPs have larger surface area when interacting with the matrix, the electrostatic charge transfer at the Pt: VO<sub>2</sub> interface is enhanced because of quantum confinement.<sup>36,37</sup> As a result, the work function of Pt NPs depends on their charge state, and Pt NPs with smaller size tend to have a reduced work function.<sup>28,38</sup> The lowest work function of Pt NPs is reported around 4.6 eV.<sup>39</sup> As shown in scenario a (**Figure 4a1, a2**), the work function of small Pt NPs is lower than that of VO<sub>2</sub> matrix before contact. When small Pt NPs and VO<sub>2</sub> form a contact, the conduction band of VO<sub>2</sub> bends upward due to the alignment of Fermi levels. Therefore, charge carriers were injected from small Pt NPs into VO<sub>2</sub> matrix, forming an electron rich region in VO<sub>2</sub> matrix near the contact interface, which further results in the  $T_c$  drop by reducing the energy barrier for phase transition. However, in scenario b (**Figure 4b1, b2**), when the work function of large Pt NPs is higher than that of VO<sub>2</sub> matrix before contact, the conduction band of VO<sub>2</sub> bends downward when VO<sub>2</sub> matrix forming contact with large Pt NPs. The consequent charge carrier depletion region in VO<sub>2</sub> matrix near the contact interface will decrease the electron density of the VO<sub>2</sub> matrix and further increase the  $T_c$ . The second major factor for bidirectional  $T_c$  tuning is the change of Pt NPs size and in turn, the variation of the Pt: VO<sub>2</sub> phase boundary density. Smaller NPs tend to have more interface area with the VO<sub>2</sub> matrix, which prompts an increase of overall electron density in the VO<sub>2</sub> matrix.<sup>27</sup> The increase in the Pt: VO<sub>2</sub> phase boundary density with smaller NPs results in a continuous drop of  $T_c$ . On the other hand, film strain introduced by the film-substrate lattice mismatch could also play a role in the  $T_c$  of VO<sub>2</sub> films as previously reported.<sup>17-19</sup> Since VO<sub>2</sub> (M1) (020) peak in all Pt: VO<sub>2</sub> films shows a very minor shift in the same

direction with respect to the pure VO<sub>2</sub> (M1) (020) peak, suggesting that the strain effect is minimal on the  $T_c$  tuning for this case.

Based on the above results, the bidirectional  $T_c$  tuning of VO<sub>2</sub> can be effectively achieved by controlling the size of Pt NPs. Small Pt NPs cause upward band bending of VO<sub>2</sub> and large interface area with VO<sub>2</sub>, both leading to the increase of charge carrier density and further  $T_c$  drop. On the other hand, large Pt NPs can result in two competing factors, downward band bending of VO<sub>2</sub> to increase  $T_c$  while small interface area to decrease  $T_c$ . The two competing factors thus lead to  $T_c$  increase for large Pt NPs. The proposed mechanism also explains the smaller difference in  $T_c$  increase than  $T_c$  decrease.

Both dielectric permittivity  $\varepsilon'$  (real part) of Pt: VO<sub>2</sub> films at 25 °C and at 90 °C are plotted in **Figure 5a, b**. The dielectric permittivity  $\varepsilon''$  (imaginary part) are plotted in Figure S4a, b in the supporting information. The angular dependent spectroscopic ellipsometry measurement assumes isotropic response of the films. General oscillator models were used in accordance with Kramers-Kronig consistence. Lorentz model was used for room temperature (25 °C) measurement and Drude-Lorentz model was used for elevated temperature (90 °C) measurement. The  $\varepsilon'$  of Pt: VO<sub>2</sub> films stays positive at room temperature, which is consistent with the semiconducting behaviors observed in R-T measurement. At the low frequency (long wavelength) end, the nanocomposite film with small Pt NPs shows relatively low  $\varepsilon'$  value, which is also in accordance with high conductivity and electron density as discussed. On the other hand, Pt: VO<sub>2</sub> films behave metallic after phase transition at 90 °C, which is depicted by negative  $\varepsilon'$  value in the near-infrared region. Moreover, the size of Pt NPs shows the tunability of the epsilon-near-zero (ENZ) wavelength. The red shift of ENZ wavelength implies the decrease of free carrier density with small Pt NPs after phase transition.

The UV-vis-NIR transmittance spectra of all Pt: VO<sub>2</sub> films and pure VO<sub>2</sub> film are shown in **Figure 5 c, d**. The absorption peak of Pt NPs is not visible due to its high frequency of surface-plasmon resonance (SPR). The corresponding Tauc plot is also shown as an inset in **Figure 5c** to calculate the bandgap of VO<sub>2</sub>. As shown in **Figure 5d**, the bandgap of Pt: VO<sub>2</sub> films varies from 1.42 eV (size of Pt  $\approx$  1.56 nm) to 2.08 eV (size of Pt  $\approx$  4.26 nm). The bandgap of pure VO<sub>2</sub> film deposited at 500 °C was plotted as a solid line for reference. The calculated value is comparable to the optical constants available in the literature.<sup>40</sup> Compared to the pure VO<sub>2</sub> film, The increase and decrease in  $E_g$  is in accordance with the energy band structure reconstruction induced by Pt NPs, as illustrated in **Figure 4a1-b1**. The upward bending of VO<sub>2</sub> conduction band with small Pt NPs leaves an electron rich region in VO<sub>2</sub> while the downward bending of VO<sub>2</sub> conduction band with large Pt NPs leaves an electron deficient region in VO<sub>2</sub>. The tunability of bandgap is thus achieved by changing electron density in the VO<sub>2</sub> matrix.

Taking advantage of the novel Pt: VO<sub>2</sub> nanocomposite design, the demonstration of bidirectional  $T_c$  tuning provides a potential candidate for VO<sub>2</sub>-based novel electronics and photonics applications operating under specific temperatures. First, compared to the prior metallic doping approach,<sup>20-23</sup>  $T_c$  can be systematically tuned in a broad temperature range via single metal selection in this work. The degradation of phase transition properties at high doping level,<sup>24,25</sup> from which metallic doping approach suffers, is also effectively mitigated by the high quality films via Pt: VO<sub>2</sub> nanocomposite design. Second, the unique Pt: VO<sub>2</sub> nanocomposite was processed by using a single-step PLD method to achieve bidirectional  $T_c$  tuning. This is different from the Pt/VO<sub>2</sub> bilayered films previously reported to achieve  $T_c$  around 332 K and 345 K depending on the substrate selection and deposition technique.<sup>41,42</sup> Very recently, Jian *et al.* proposed a combination of metal selection and NP size control to achieve a record low  $T_c$  of 301.8 K.<sup>27</sup> The novelty of this work

lies in that, using tunable metal nanoparticle size, a single metal doping selection can achieve bidirectional  $T_c$  tuning over a broad range. As a result of the size dependent work function tunability of Pt NPs, the feasibility of bidirectional  $T_c$  tuning was achieved by Pt: VO<sub>2</sub> nanocomposite design and potentially other metal: VO<sub>2</sub> nanocomposites, providing candidates for temperature sensors and thermal switches under elevated temperatures.

## Conclusions

Bidirectional tuning of the metal-insulator transition temperature ( $T_c$ ) in VO<sub>2</sub> has been demonstrated via the Pt: VO<sub>2</sub> nanocomposite design. Pt NPs were uniformly distributed in the VO<sub>2</sub> matrix, with NP size ranging from 1.56 to 4.26 nm due to the growth temperature variation.  $T_c$  is effectively and systematically tuned from 329.16 to 360.74 K as compared to 345.72 K for pure VO<sub>2</sub> film. Optical properties, including transmittance ( $T\%$ ), dielectric permittivity ( $\epsilon'$ ), and epsilon-near-zero (ENZ) wavelength were also effectively tuned because of the Pt NPs. The mechanism for bidirectional phase transition tuning is mainly attributed to two factors: the reconstruction of band structure at the Pt: VO<sub>2</sub> interface and the change of Pt: VO<sub>2</sub> phase boundary density. Small Pt NPs bend the VO<sub>2</sub> conduction band upwards and have large interface area with VO<sub>2</sub>, both of which increase the charge carrier density and result in the  $T_c$  drop. On the other hand, large Pt NPs bend the VO<sub>2</sub> conduction band downwards to increase  $T_c$  while having small interface area to decrease  $T_c$ , thus partially depleting the charge carrier and causing  $T_c$  to increase. This study provides a promising approach towards practical VO<sub>2</sub>-based device applications as novel electronics and photonics under specific operation temperatures.

## Conflicts of interest

There are no conflicts to declare.

## Acknowledgements

The authors thank the support from the U.S. National Science Foundation (DMR-1809520) for thin film deposition, structural and property characterizations and (DMR-1565822) for high resolution STEM/EDX analysis.

## Reference

- 1 A. Zylbersztein and N. F. Mott, *Phys. Rev. B*, 1975, **11**, 4383–4395.
- 2 N. F. Mott, *Rev. Mod. Phys.*, 1968, 40, 677–683.
- 3 M. Cyrot, *J. Phys.*, 1972, **33**, 125–134.
- 4 F. J. Morin, *Phys. Rev. Lett.*, 1959, **3**, 34.
- 5 J. B. Goodenough, *J. Solid State Chem.*, 1971, **3**, 490–500.
- 6 M. Imada, A. Fujimori and Y. Tokura, *Rev. Mod. Phys.*, 1998, **70**, 1039.
- 7 V. Eyert, *Ann. Phys.*, 2002, **11**, 650–704.
- 8 P. Miao, J. Wu, Y. Du, Y. Sun and P. Xu, *J. Mater. Chem. C*, 2018, **6**, 10855–10860.
- 9 D. Ruzmetov and S. Ramanathan, *Thin Film Metal-Oxides: Fundamentals and Applications in Electronics and Energy*, 2010, 51–94.
- 10 M. Liu, H. Y. Hwang, H. Tao, A. C. Strikwerda, K. Fan, G. R. Keiser, A. J. Sternbach, K. G. West, S. Kittiwatanakul, J. Lu, S. A. Wolf, F. G. Omenetto, X. Zhang, K. A. Nelson and R. D. Averitt, *Nature*, 2012, **487**, 345–348.

- 11 J. J. Yang, M. D. Pickett, X. Li, D. A. A. Ohlberg, D. R. Stewart and R. S. Williams, *Nat. Nanotechnol.*, 2008, **3**, 429–433.
- 12 J. Homola, *Chem. Rev.*, 2008, **108**, 462–493.
- 13 T. D. Manning, I. P. Parkin, M. E. Pemble, D. Sheel and D. Vernardou, *Chem. Mater.*, 2004, **16**, 744–749.
- 14 E. E. Chain, *Appl. Opt.*, 1991, **30**, 2782.
- 15 L. Wang, Y. Yang, J. Zhao, B. Hong, K. Hu, J. Peng, H. Zhang, X. Wen, Z. Luo, X. Li and C. Gao, *J. Appl. Phys.*, 2016, **119**, 145301.
- 16 T. H. Yang, R. Aggarwal, A. Gupta, H. Zhou, R. J. Narayan and J. Narayan, *J. Appl. Phys.*, 2010, **107**, 053514.
- 17 H. Koo, S. Yoon, O. J. Kwon, K. E. Ko, D. Shin, S. H. Bae, S. H. Chang and C. Park, *J. Mater. Sci.*, 2012, **47**, 6397–6401.
- 18 J. Jian, A. Chen, Y. Chen, X. Zhang and H. Wang, *Appl. Phys. Lett.*, 2017, **111**, 153102.
- 19 D. C. Sayle and G. W. Watson, *Phys. Chem. Chem. Phys.*, 2000, **2**, 5491–5499.
- 20 N. Wang, S. Liu, X. T. Zeng, S. Magdassi and Y. Long, *J. Mater. Chem. C*, 2015, **3**, 6771.
- 21 B. Chen, D. Yang, P. A. Charpentier and M. Zeman, *Sol. Energy Mater. Sol. Cells*, 2009, **93**, 1550–1554.
- 22 T. D. Manning, I. P. Parkin, C. Blackman and U. Qureshi, *J. Mater. Chem.*, 2005, **15**, 4560–4566.
- 23 X. Tan, W. Liu, R. Long, X. Zhang, T. Yao, Q. Liu, Z. Sun, Y. Cao and S. Wei, *J. Phys. Chem. C*, 2016, **120**, 28163–28168.
- 24 H. Wang, J. Jian, W. Zhang, C. Jacob, A. Chen, H. Wang and J. Huang, *Appl. Phys. Lett.*, 2015, **107**, 102105.

- 25 L. L. Fan, Y. F. Wu, C. Si, C. W. Zou, Z. M. Qi, L. B. Li, G. Q. Pan and Z. Y. Wu, *Thin Solid Films*, 2012, **520**, 6124–6129.
- 26 G. Fu, X. Ning, M. Chen, S. Wang, P. Liu, J. Wang and X. Li, *J. Am. Ceram. Soc.*, 2019, **102**, 2761–2769.
- 27 J. Jian, X. Wang, S. Misra, X. Sun, Z. Qi, X. Gao, J. Sun, A. Donohue, D. G. Lin, V. Pol, J. Youngblood, H. Wang, L. Li, J. Huang and H. Wang, *Adv. Funct. Mater.*, 2019, **29**, 1903690.
- 28 N. T. Khoa, S. W. Kim, D. H. Yoo, E. J. Kim and S. H. Hahn, *Appl. Catal. A Gen.*, 2014, **469**, 159–164.
- 29 L. Vitos, A. V. Ruban, H. L. Skriver and J. Kollár, *Surf. Sci.*, 1998, **411**, 186–202.
- 30 J. Narayan and V. M. Bhosle, *J. Appl. Phys.*, 2006, **100**, 103524.
- 31 R. Lopez, T. E. Haynes, L. A. Boatner, L. C. Feldman and R. F. Haglund, *Phys. Rev. B*, 2002, **65**, 224113.
- 32 D. Gu, S. K. Dey and P. Majhi, *Appl. Phys. Lett.*, 2006, **89**, 82907.
- 33 C. Ko, Z. Yang and S. Ramanathan, *ACS Appl. Mater. Interfaces*, 2011, **3**, 3396–3401.
- 34 L. Zhou and M. R. Zachariah, *Chem. Phys. Lett.*, 2012, **525–526**, 77–81.
- 35 D. M. Wood, *Phys. Rev. Lett.*, 1981, 46, 749.
- 36 L.-S. Li, J. Hu, W. Yang and A. P. Alivisatos, *Nano Lett.*, 2001, **1**, 349–351.
- 37 Y. Zhang, O. Pluchery, L. Caillard, A. F. Lamic-Humblot, S. Casale, Y. J. Chabal and M. Salmeron, *Nano Lett.*, 2015, **15**, 51–55.
- 38 H. Zheng, Y. Zhou and S. Gangopadhyay, *J. Appl. Phys.*, 2015, **117**, 024504.
- 39 J. K. Schaeffer, L. R. C. Fonseca, S. B. Samavedam, Y. Liang, P. J. Tobin and B. E. White, *Appl. Phys. Lett.*, 2004, **85**, 1826–1828.

- 40 S. Y. Li, N. R. Mlyuka, D. Primetzhofer, A. Hallén, G. Possnert, G. A. Niklasson and C. G. Granqvist, *Appl. Phys. Lett.*, 2013, **103**, 161907.
- 41 L. Kang, Y. Gao, Z. Chen, J. Du, Z. Zhang and H. Luo, *Sol. Energy Mater. Sol. Cells*, 2010, **94**, 2078–2084.
- 42 J. Sakai, M. Zaghrioui, V. Ta Phuoc, S. Roger, C. Autret-Lambert and K. Okimura, *J. Appl. Phys.*, 2013, **113**, 123503.

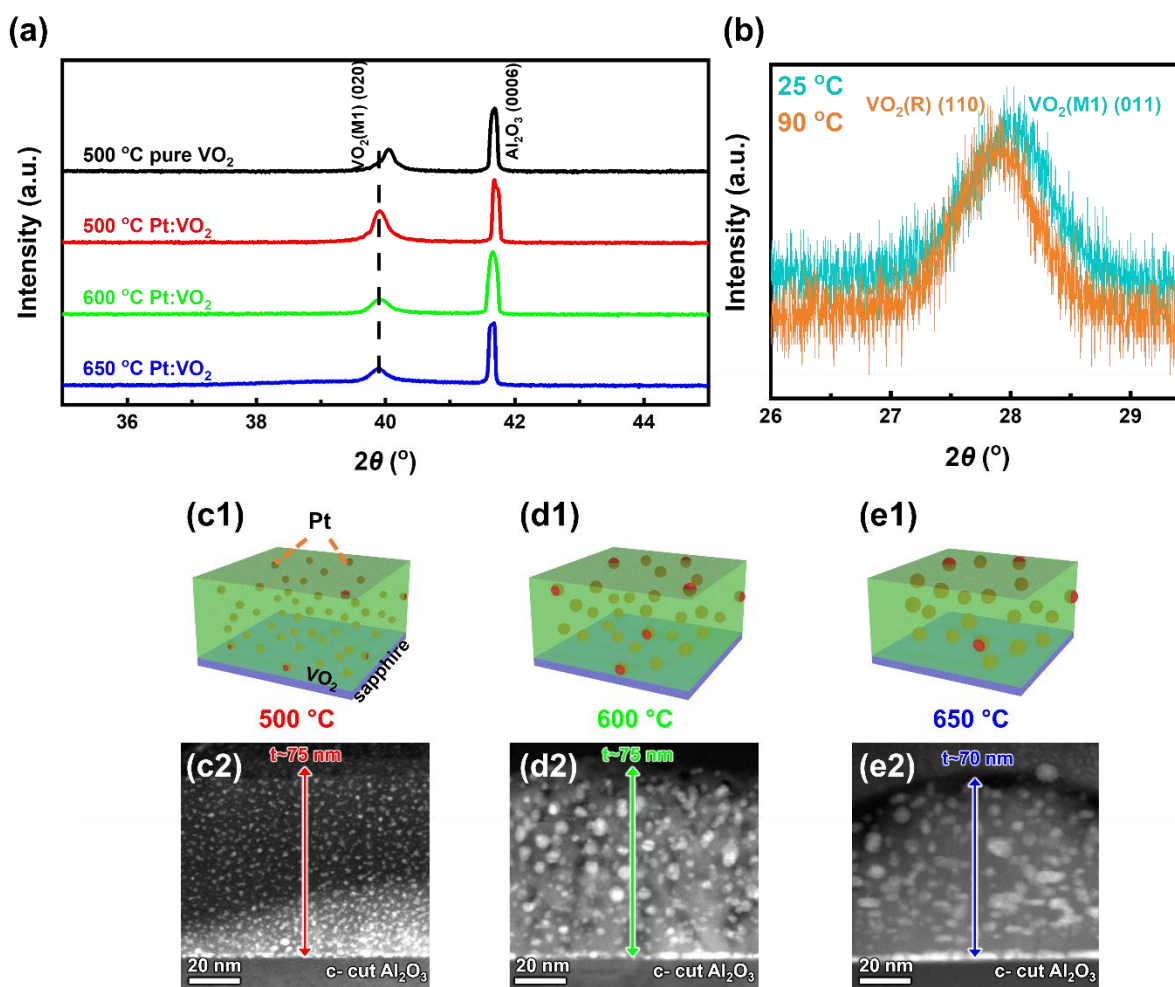


**Figure 1.** (a) XRD  $\theta-2\theta$  spectra of pure VO<sub>2</sub> film and Pt: VO<sub>2</sub> nanocomposite thin films on c-cut sapphire substrates. (b) XRD  $\phi$ -scans at 25 °C and 90 °C for 500 °C deposited Pt: VO<sub>2</sub>

nanocomposite thin films. (c1, d1, e1) Schematic diagram of the temperature dependence of Pt: VO<sub>2</sub> nanocomposite thin films grown on c-cut sapphire. Size control is possible through temperature control in pulsed laser deposition (PLD). (c2, d2, e2) STEM cross-section images of the Pt: VO<sub>2</sub> nanocomposite thin films deposited at 500, 600, and 650 °C, respectively.

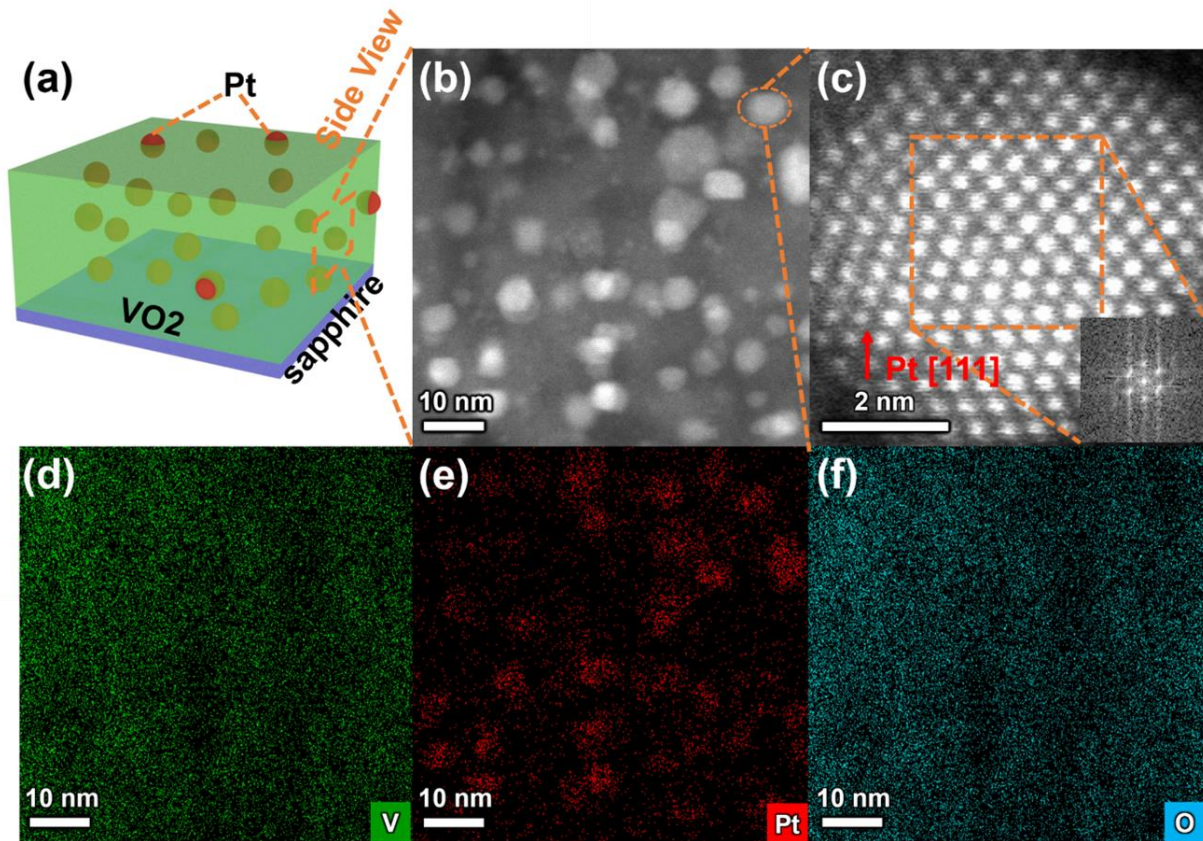


**Figure 2.** (a) Schematic diagram and (b) low-magnification STEM cross-section image of 650 °C deposited Pt: VO<sub>2</sub> nanocomposite thin films. (c) High-resolution STEM image of the Pt NP labeled in (b) and its corresponding FFT pattern. (d, e, f) Cross-section EDS mapping of V, Pt and O elements in the Pt: VO<sub>2</sub> nanocomposite thin films.

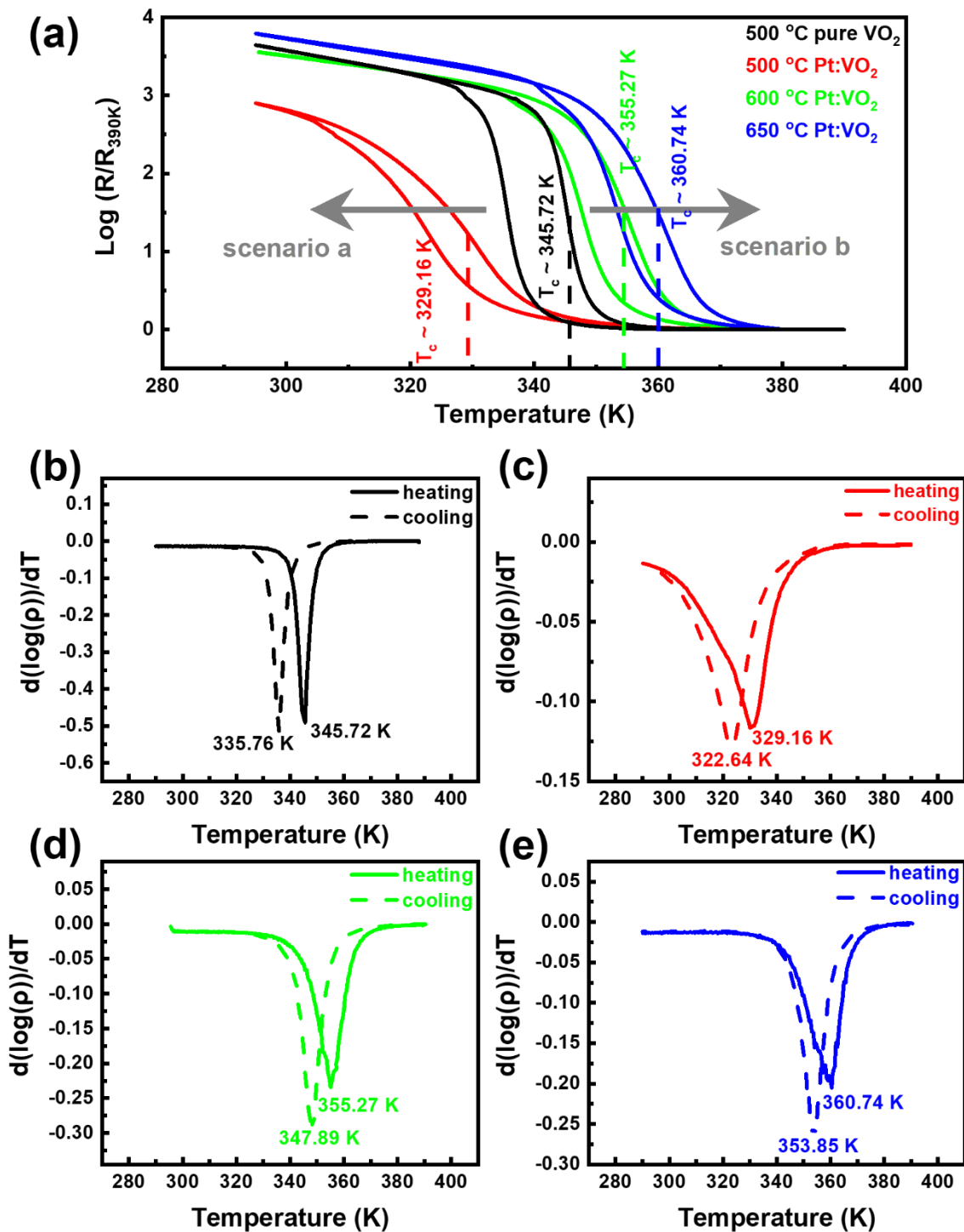


**Figure 3.** (a) Normalized resistivity-temperature plots of the Pt: VO<sub>2</sub> nanocomposite thin films deposited at 500, 600, and 650 °C, respectively. (b-e) Resistivity changing rate of pure VO<sub>2</sub> films and Pt: VO<sub>2</sub> films deposited at 500, 600, and 650 °C, respectively.

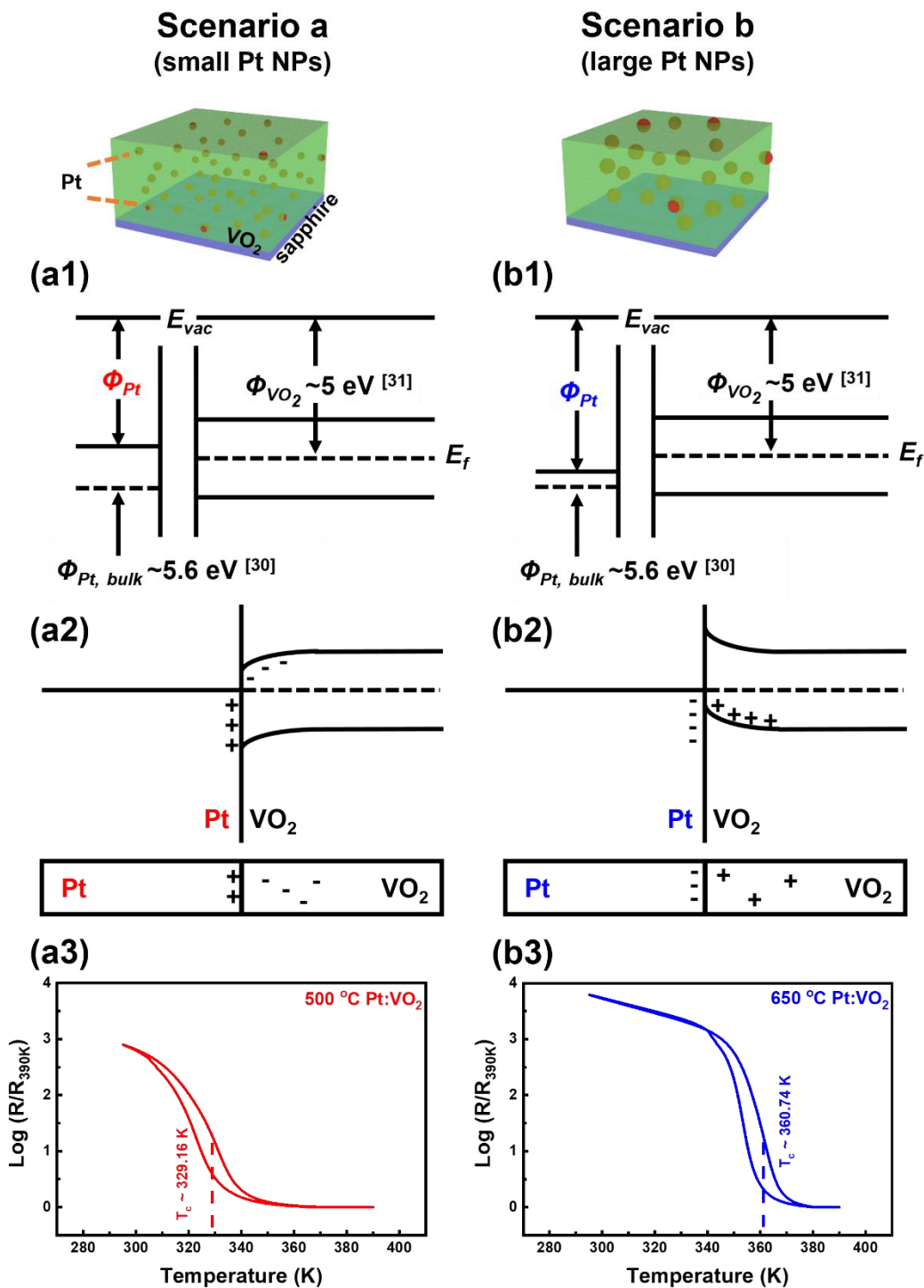


**Figure 4.** Band diagram of small Pt NPs and VO<sub>2</sub> (a1) separately (a2) when forming contacts in scenario a. (a3) Normalized resistivity-temperature plot of the 500°C deposited Pt: VO<sub>2</sub>

nanocomposite thin film. Band diagram of large Pt NPs and VO<sub>2</sub> (b1) separately (b2) when forming contacts in scenario b. (b3) Normalized resistivity-temperature plot of the 650 °C deposited Pt: VO<sub>2</sub> nanocomposite thin film.

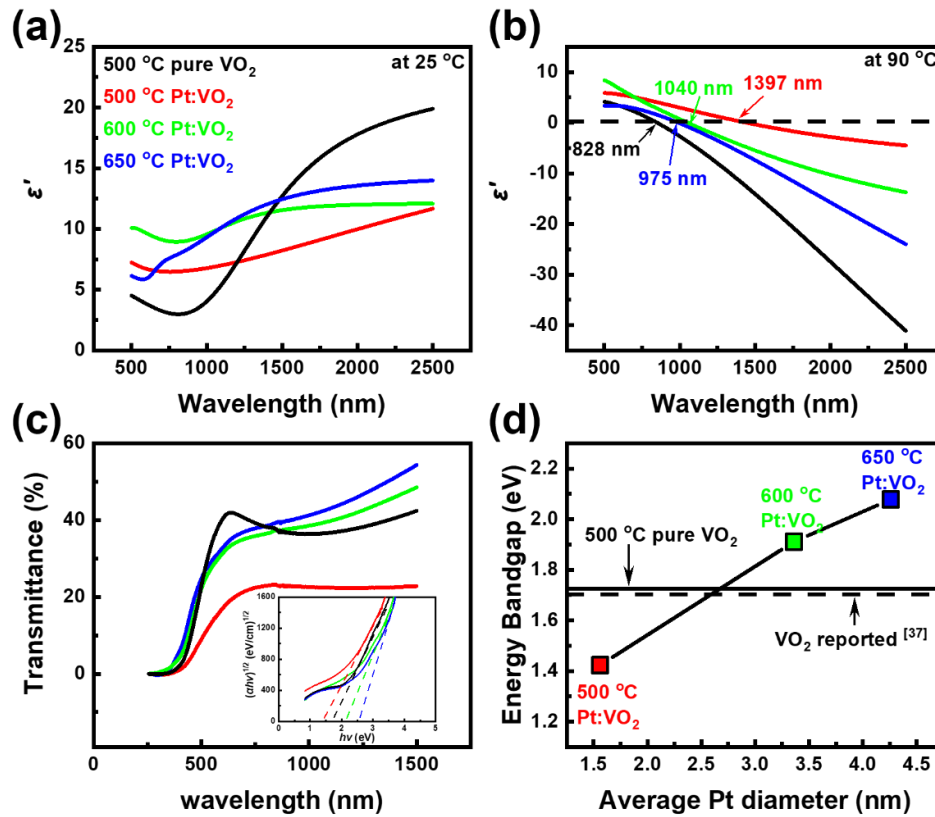


**Figure 5.** The real part of dielectric permittivity  $\epsilon'$  (a) at 25 °C and (b) at 90 °C for Pt: VO<sub>2</sub> nanocomposite thin films deposited at 500, 600, and 650 °C, respectively. (c) Optical transmittance ( $T\%$ ) spectra of the Pt: VO<sub>2</sub> nanocomposite thin films deposited at 500, 600, and 650 °C, respectively. The inset is the Tauc plot for all Pt: VO<sub>2</sub> films. (d) Tunable energy bandgap of all Pt: VO<sub>2</sub> films as a function of NP size.

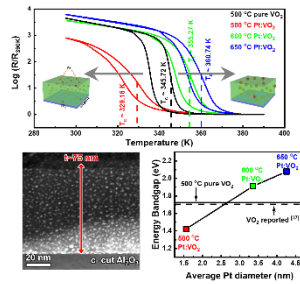
**Table 1.** SMT characteristics of the as-deposited pure VO<sub>2</sub> film and Pt: VO<sub>2</sub> films.

	Deposition temperature (°C)	$T_c$ (K)	$\Delta A$	$\Delta T$ (K)	$\Delta H$ (K)	$R_{260K} (\times 10^4 \Omega)$
Pt: VO <sub>2</sub>	500	329.16	6191	12.8	6.52	1.16
	600	355.27	7758	9.7	7.38	3.64
	650	360.74	8765	10.1	6.89	6.33
Pure VO <sub>2</sub>	500	345.72	11759	7.5	9.96	12.25

## Table of Contents Entry

### Bidirectional tuning of phase transition properties in Pt: VO<sub>2</sub> nanocomposite thin films

Zihao He<sup>a</sup>, Jie Jian<sup>b</sup>, Shikhar Misra<sup>b</sup>, Xingyao Gao<sup>b</sup>, Xuejing Wang<sup>b</sup>, Zhimin Qi<sup>b</sup>, Bo Yang<sup>b</sup>, Di Zhang<sup>b</sup>, Xinghang Zhang<sup>b</sup>, Haiyan Wang<sup>a,b\*</sup>



Pt: VO<sub>2</sub> nanocomposite design to achieve bidirectional tuning of phase transformation via size dependent work function of nanoparticles.